OVERLAY

Journal of Theoretical,
Computational and
Applied Mechanics

DIAMOND OPEN ACCESS

Identifiers
DOI 10.46298/jtcam.7062
OAI hal-03101377v2

History
Received Jan 8, 2021
Accepted Jan 25, 2022
Published May 5, 2022

Associate Editor
Julien Réthoré

Reviewers
Anonymous
Anonymous

Open Review
OAI hal-03566740

Rate dependency and ply thickness influence on transverse cracking evolution in cross-ply laminates

Fabien Coussa[1], **Julien Berthe**[1,2], and **Matthieu Ragonet**[1]

[1] ONERA, Materials and Structures Department / Design & Dynamic Resistance Research Unit, 5 rue des Fortifications, CS 90013, F-59045 Lille Cedex, France
[2] Université de Lille, CNRS, Centrale Lille, UMR 9013-LaMCube, Laboratoire de Mécanique, Multiphysiques, Multiéchelles, F-59000 Lille, France

The present work investigates the rate dependency of transverse cracking evolution in cross-ply laminates for various 90° plies thicknesses. The crack detection methodology is based on a recently proposed protocol relying on the use of infrared thermography. A new analysis methodology makes it more robust and to directly links the spatial localization of the crack with the stress level at which it occurs. The corresponding results for various loading rates and 90° ply thicknesses are analysed. The crack density evolution with respect to stress apply to the laminate exhibits a rate dependency only for the $[0/90]_s$ configuration. This rate dependency is finally discussed based on transverse crack onset theories in cross-ply laminates.

Keywords: Transverse cracking, Rate dependency, Infrared thermography, Composite materials

1 Introduction

The increased use of composite materials in transport industries and in applications to structural parts has motivated the use of a wide range of experimental techniques to analyse the degradation mechanisms by matrix cracking under different kinds of loadings. In the range of low and quasi-static loading rates, the analysis of the cracking density in cross-ply laminate has been the subject of numerous studies (Crossman et al. 1980; Dzenis 2003; Farge et al. 2010). Most of these techniques have been used under cyclic loadings where the interruption of the test allows the observation and the measurement of the material degradation mechanisms for various loading levels. For the dynamic speed range, however, such protocols are limited due to the open-loop control of the testing machine. Difficulties related to the interruption of loading before the specimen failure is still considered as a real limit to this type of analysis. In the present work, a non-intrusive measurement technique using infrared (IR) thermography is used in order to analyse the effect of the loading-rate increase on the evolution of the cracking density as a function of the applied stress. This approach has already been used to measure the evolution of damage in composites subject to quasi-static loadings (Lisle et al. 2013; Montesano et al. 2014), fatigue loadings (Toubal et al. 2006; Li et al. 2016) and more recently to loadings at intermediate dynamic loading-rate (Battams and Dulieu-Barton 2016). However, the detection and the quantification by IR thermography of transverse cracks for dynamic loads remains little investigated in the literature due to the limitations on the acquisition frequency of the older generation of IR cameras. The present work proposes to extend the analysis performed in the quasi-static ranges in Berthe and Ragonet (2018) to a dynamic loading-rate range, through the use of a high-rate IR camera (Telops FAST M3K).

In the sequel, the experimental procedure is first introduced in order to present the material of the study and the experimental setup. Then, an innovative analysis procedure is proposed and applied on tests performed at various loading rates. Finally, this procedure is applied on experimental results to analyse the loading-rate influence for various 90° ply thicknesses.

2 Experimental procedure

2.1 Material and specimens

The material considered in this study is the unidirectional prepreg HexPly M21/35%/268/T700GC (Hexcel France) made of T700 carbon fibres and M21 epoxy resin. The impact resistance performance of this material has been enhanced by means of the inclusion of thermoplastic nodules in the epoxy resin. Laminate plates have been manufactured by hand lay-up. A typical cure cycle has been performed in an autoclave. Different symmetric and balanced stacking sequences have been chosen: $[0/90_3]_s$, $[0/90_2]_s$, $[0/90]_s$ and $[0/90_{1/2}]_s$. Rectangular specimens were cut out of plates using a water-cooled diamond saw with the following dimensions: 15 mm wide and a free length ℓ_0 of 41 mm between the GFRP tabs with an approximate length of about 50 mm. The different specimen thicknesses are respectively associated with the different stacking sequences as follows: 2.15 mm, 1.61 mm, 1.08 mm and 0.81 mm.

2.2 Test setup

The experimental environment for the whole experimental investigation is illustrated in Figure 1. Every test has been performed by means of the use of a SCHENCK servohydraulic jack. This test facility allows to apply on the specimen various constant upper holder speeds from 5 mm/min to 10 m/s. This study is focused on five different upper holder speeds: 5 mm/min, 50 mm/min, 500 mm/min, 0.1 m/s and 1.4 m/s. The objective is to finely cover a wide range of theoretical strain-rates from quasi-static range of $\dot{\varepsilon} = 2 \times 10^{-3}\ \mathrm{s}^{-1}$ to an intermediate dynamic range of $\dot{\varepsilon} = 35\ \mathrm{s}^{-1}$. The measurement of the applied load is performed by a piezoelectric load-cell (Kistler 9071A). A pre-loading has been applied in order to be able to measure loads between −200 kN and 200 kN. The measurement of the upper holder displacement is performed by means of a laser transducer (Keyence LK-HD500 and LK-H052) in order to be able to accurately capture the real speed applied to the specimen. The specimen longitudinal strain is measured using a non-contact technique to avoid any disturbance of the measurement that could be generated by the appearance of cracks (Berthe and Ragonet 2018). An optical extensometer Rudolph 200XR is used to capture two black-and-white transitions painted on the specimen surface. The two transitions are separated by a distance ℓ of about 32 mm. The distance ℓ has been precisely measured for each specimen before each test. In addition, a Telops Fast M3k infrared camera with a 50 mm lens is used to monitor the temperature evolution of the edge surface of the free length of the samples. The camera sensor allows to capture an image of 320 × 256 pixels up to 3.1 kHz in full frame an up to 100 kHz with a reduced spatial resolution of 64 × 4 pixels. Transverse crack

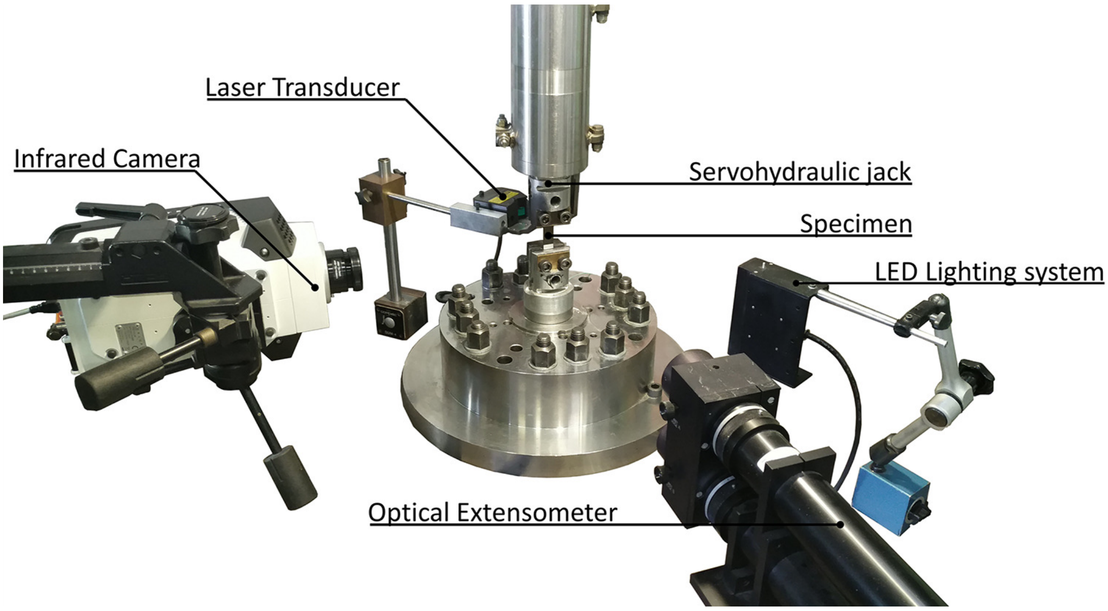

Figure 1 Experimental set-up suitable for the static and dynamic strain-rate range

propagation in $[0_m/90_n]_s$ can be considered as almost instantaneous from side to side (Berthelot 2003; Huchette 2005). This hypothesis remains valid with the loading rate increase (Berthe and Ragonet 2018). Based on this assumption, only one edge of the different specimens has been monitored to maximize the IR camera frame-rate for the high loading-rate tests. More information about the camera acquisition parameters and the image analysis will be given in Section 2.3. At last, the synchronization of each measurement system and the data acquisition are performed by means of a Dewetron DEWE-2600 acquisition system at 1 MHz. For each configuration *i.e* every stacking sequences and loading rates, a minimum of three tests is performed in order to evaluate discrepancies between tests.

2.3 Crack detection based on infrared thermography for dynamic loadings

The protocol used in this study is based on a detection procedure which has been proposed by Berthe and Ragonet (2018). The extension of this methodology to thinner 90° plies and to higher loading rates will be studied in the sequel. The crack detection using an infrared camera relies on the fact that the occurrence of some dissipative mechanisms such as matrix cracking leads to a local modification of the infrared radiation of the observed body. This modification associated to the local heat dissipation of the mechanism is directly related to a local temperature variation. A pixel-by-pixel calibration may be performed in order to conduct an accurate and a quantitative measurement as in Berthe's works, where one hundred images of a black body surface were captured every 0.5 °C between 20 °C and 29 °C. In this study, we use the Telops' factory pre-calibration which is valid for the Janos Asio 50 mm lens over the wavelength 3–5 µm and defined over a temperature range between 0 °C and 178 °C and for various integration times. The objective is not to obtain an accurate measurement of the absolute temperature, as the detection technique is only based on a sudden increase of the local temperature (at least 1 °C) due to crack appearance. Consequently, the manufacturer calibration is accurate enough for the purpose of this study.

The following section aims at describing the methodology employed in order to objectively quantify the evolution of crack density from quasi-static to intermediate dynamic loadings. Following the first section, an illustration of the principle is presented for the $[0/90_2]_s$ configuration. The next section is referred to the results obtained at different strain rates and for several specimen thicknesses.

3 Results and discussions

3.1 Application to the $[0/90_2]_s$ configuration

3.1.1 Tensile test performed at 5 mm/min

Following a set of several increasing levels of tensile loads applied on a $[0/90_2]_s$ specimen, Figure 2 illustrates several thermal fields referring to an apparent temperature variation ΔT, which have been captured over the whole surface of the side of the specimen.

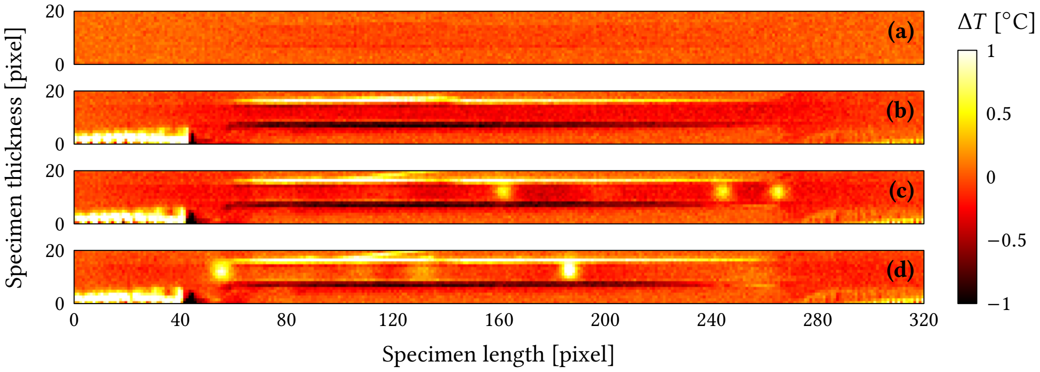

Figure 2 Variation of the temperature ΔT captured along the edge of a $[0/90_2]_s$ laminate at various load levels, for a test performed at 5 mm/min: (a) 20 % $\sigma_{\max}$, (b) 60 % $\sigma_{\max}$, (c) 80 % $\sigma_{\max}$ and (d) 95 % $\sigma_{\max}$.

The fields of the apparent temperature variation are obtained by computing the difference of two temperature fields between a time t and the time t_0 which corresponds to the beginning of the loading of the sample. This analysis methodology is classically used by various authors to focus on temperature variation due to the mechanical loading of the sample (Meola and Carlomagno 2009; Portemont et al. 2018). At the beginning of the test, the abscissa within the intervals $x = [0; 60]$ and $x = [265; 320]$ refer to the tabs length. The abscissa within the interval $x =]60; 265[$ refers to the whole free-length of the specimen. The ordinates within the interval $y = [8; 16]$ refer to the specimen thickness of the free-length, which include both the two 0° plies on the outer faces of the specimen and the four 90° plies. The specimen is submitted to an uniaxial tensile load at the lower speed of this study (5 mm/min). The acquiring frequency of the measuring load is about 10 kHz. The integration time of the infrared camera is set at 190 µs. For a 320×20 pixels picture, the IR camera frequency is defined at 500 Hz. Considering this picture configuration, a set of five pixels through the thickness of the 90° plies are used to capture the crack mechanisms.

In the first instance and due to the thermoelasticity phenomenon, an homogeneous decrease of the apparent temperature is observed over the whole free length, see Figure 2(b). With the increase of the load applied to the specimen, several strongly localized hot areas can be observed. Only located within the total thickness of the 90° plies, these hot spot areas captured by the IR camera reveal the energy dissipated as heat during the process of creation of the transverse cracking mechanism (Figure 2(c) and Figure 2(d)). A dedicated methodology for the quantification of matrix crack density using IR thermal fields and over a wide range of quasi-static tensile loads has been proposed by Berthe and Ragonet (2018). This procedure has been validated with a cross analysis of the qualitative detection of the thermal events over the time and the quantitative detection of the load signals oscillations captured by the piezoelectric load cell that have been generated by crack occurrences. The main drawback of this methodology is that it is fully based on a manual user-based analysis of the thermal fields. In order to make this analysis more robust and convenient, an automatic procedure is proposed in this study. It is based on the tracking of the thermal events along a sole line of pixels during the whole test period. The line of pixel is chosen to be located in the middle of the 90° plies and encompasses the whole free length of the sample, see Figure 3(a). From the beginning of the test until a few millisecond seconds before the final failure, Figure 3(b) depicts every recorded occurrences related to each temperature variations along the line. It can be observed that most of the captured thermal events are of the same amplitude and are diffusely spread over the entire free length with a relative constant distance between each peak. In order to consistently correlate the occurrence of thermal events with a level of applied stress, a time synchronization is required. Since the brittle failure of the

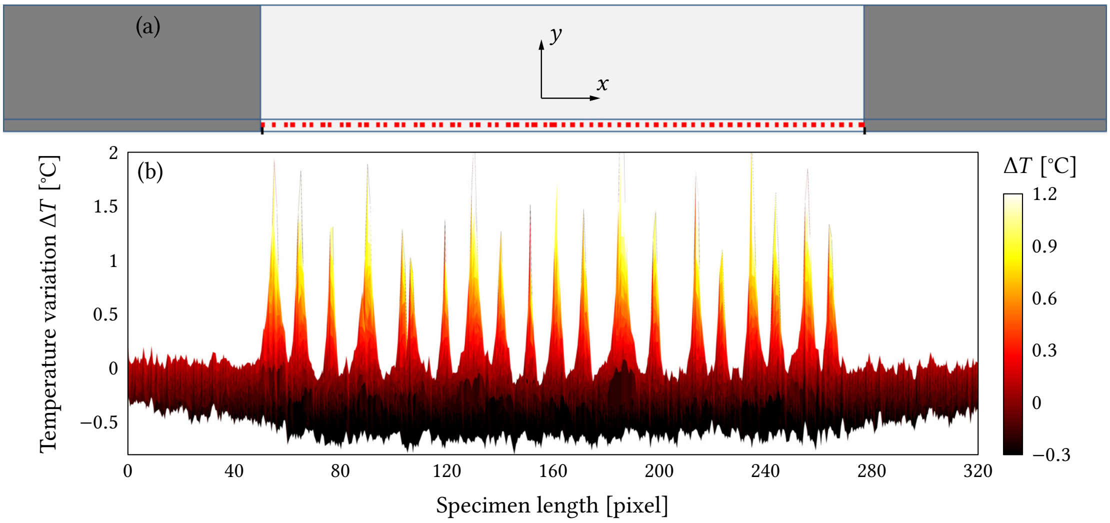

Figure 3 (a) Schematic representation of a tracked line of pixels (red dots) located in the middle of the specimen thickness and within the 90° oriented plies. (b) Captured thermal events along a line of a 320 pixels during a tensile test on a $[0/90_2]_s$ laminate at 5 mm/min.

samples results in the release of an high amount of energy, the failure phenomenon is objectively detectable on infrared images. The time synchronization is therefore based on the specimen final failure. Figure 4 provides a representative result of the proposed methodology. As shown, each crack occurrence can be directly related to the stress applied on a continuous basis. Another advantage related to this method lies in the direct access to a sole and explicit visualization of the spatial distribution of the cracks location from the beginning of the loading until the end. Concerning the considered stacking sequence and the considered loading speed, the first cracks appears for a longitudinal loading $\sigma_{xx} = 349$ MPa. Beyond this stress level, various cracks are generated within the free-length. As it can be also observed, the cracks still develop until the end of loading, which means that the crack kinematic has not reached its saturation level. In order to avoid the time-consuming nature of a manual crack count and to allow an objective quantification of crack density, an additional post-processing of the thermal pictures can be performed. A regularization of the ΔT fields can be performed using an unidirectional gradient over time. Figure 5(a) depicts the mean fields of the $\nabla\Delta T$ in function of the applied stress, where the upper and lower bounds correspond to ten times the standard deviation of the $\nabla\Delta T$ mean. By reducing the noise around the thermal events, the cracking mechanism is emphasized and can be accurately detected by means of an automatized peaks detection subroutine. Based on this methodology, accurate evolution laws of crack density can be obtained and illustrated as in Figure 5(b). The crack density is computed by means of

Figure 4 Spatial distribution of the thermal events for a test performed at 5 mm/min in a $[0/90_2]_s$ laminate.

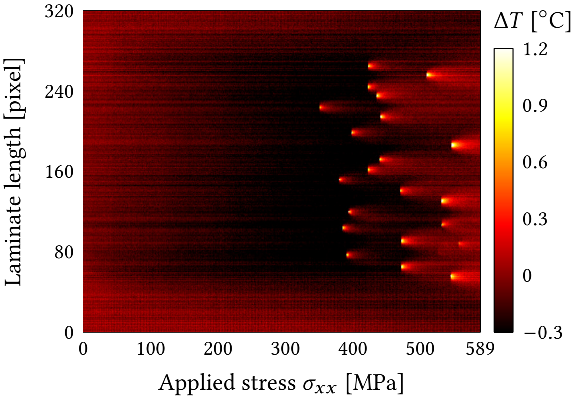

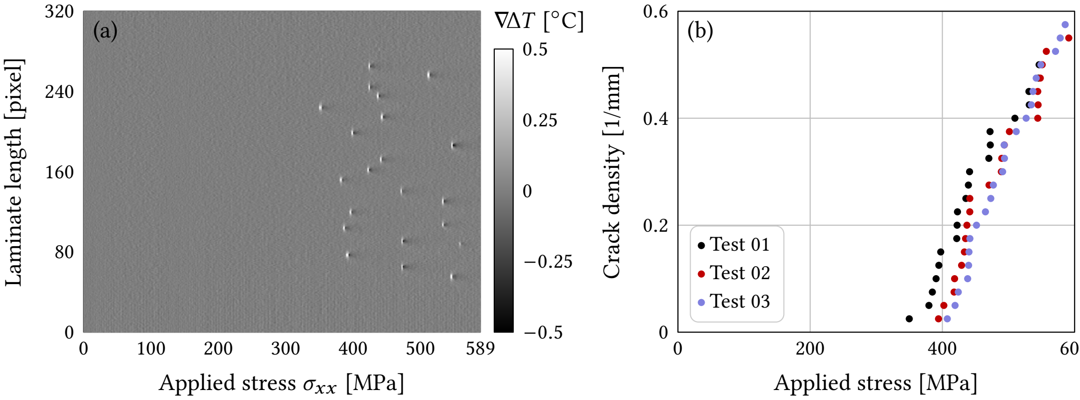

Figure 5 Cracks density d based on crack detection in infrared thermography images: (a) regularized thermal field for Test 01 and (b) quantification of the crack density for tests performed at 5 mm/min.

$$d = N_c/\ell_0 \tag{1}$$

with N_c the number of transverse cracks counted in the 90° plies. A reliable applied stress is obtained for each generated crack. For the three performed tests, this procedure leads to low discrepancies results, with a mean value of $\sigma_{\text{onset}} = 383 \pm 30$ MPa regarding the stress threshold of the crack onset. The evolution of the crack kinetics is found to be similar between the three tests. A mean value of the maximum crack density $d_{\max} = 0.54 \pm 0.04$ is obtained for an average $\sigma_{xx}^{d_{\max}} = 574.42 \pm 24.5$ MPa. A mean value of $\sigma_{xx} = 602.45 \pm 11.9$ MPa is measured for the maximum stress applied to the laminate.

3.1.2 Tensile tests performed at various loading rates

One of the main objectives of the study is to assess the reliability of the proposed methodology to be applied for high speed tensile tests. As mentioned in Section 2.2, five loading speeds are considered. For each considered loading speed and each stacking sequence configuration, the infrared camera parameters are summarized in Table 1 as well as the induced uncertainty associated with the crack occurrence detection.

Loading rates	Resolution [px^2]	Integration time [µs]	IR Frame-rate [Hz]	Time uncertainty [s]	Stress uncertainty [MPa]
5 mm/min	320 × 20	190	500	2×10^{-3}	$\leqslant 0.1$
50 mm/min	320 × 20	180	4000	2.5×10^{-4}	$\leqslant 0.2$
500 mm/min	256 × 16	180	5000	2×10^{-4}	$\leqslant 0.7$
0.1 m/s	256 × 16	180	5000	2×10^{-4}	$\leqslant 7$
1.4 m/s	256 × 12	60–15	15000–30000	6.7×10^{-5}–3.4×10^{-4}	$\simeq 50$

Table 1 Infrared camera parameters used for the experimental investigation from static to intermediate dynamic loadings.

It can be noticed that the integration time remains overall constant regardless of the loading rate. To reach a higher acquisition frequency for the test performed at 1.4 m/s, the integration time for these tests has to be reduced. An integration time of 15 µs is used for the $[0/90_3]_s$ and $[0/90_2]_s$ laminate configurations. An integration time of 60 µs is used for the thinner laminate configurations $[0/90_1]_s$ and $[0/90_{1/2}]_s$ to increase the sensitivity of the measurement for these configuration where crack detection can be more difficult. Based on the procedure described in Section 3.1.1, Figures 6 to 9 illustrate the capability of the protocol to capture and to quantify crack mechanisms over a large range of strain rates regarding the $[0/90_2]_s$ laminate configuration.

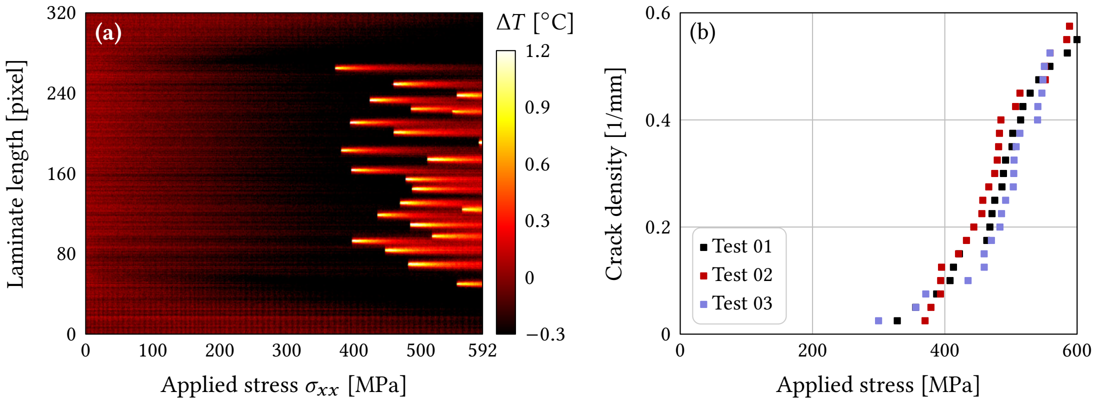

Figure 6 Crack density for a $[0/90_2]_s$ laminate subject to tensile tests performed at 50 mm/min: (a) captured thermal events for Test 02 and (b) crack kinetics.

It should be mentioned that although a reduction in spatial resolution is required for high-speed loadings, the number of effective pixels in the thickness of the 90° layers remains fixed at five pixels. First, Figures 6(a), 7(a), 8(a) and 9 illustrate the ability of the experimental protocol to capture the cracking mechanism and to associate it directly with the applied stress is demonstrated over a wide range of quasi-static and dynamic loading rates. For the last loading rate considered in the present study, although it is possible to qualitatively capture the presence and the spatial distribution of the cracking mechanism, the low temporal sampling (only five images were acquired during the whole loading) does not allow a continuous and consistent quantification of the cracking kinetics. This loading rate is therefore withdrawn for the rest of the analysis in the sequel of the study. This loading rate can be considered as a limit of this experimental investigation due to the current acquiring frequency of IR cameras. Second, Figures 6(b), 7(b) and

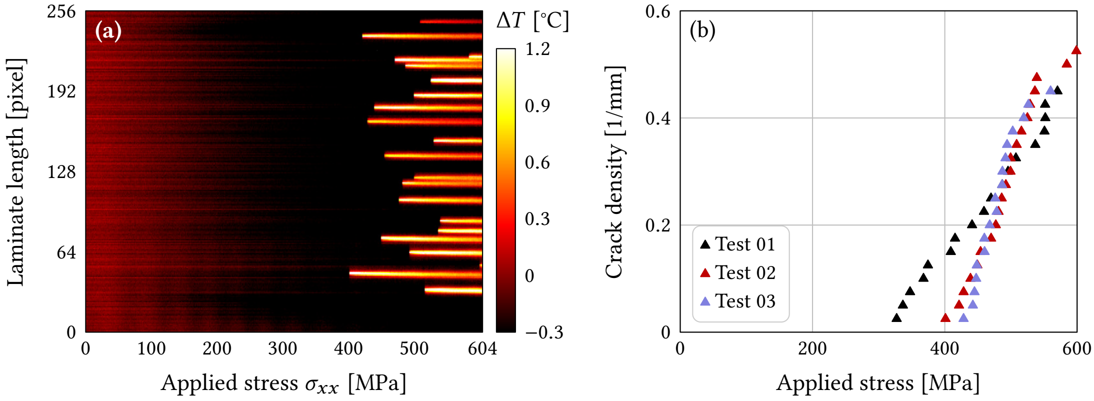

Figure 7 Crack density for a $[0/90_2]_s$ laminate subject to tensile tests performed at 500 mm/min: (a) captured thermal events for Test 02 and (b) crack kinetics.

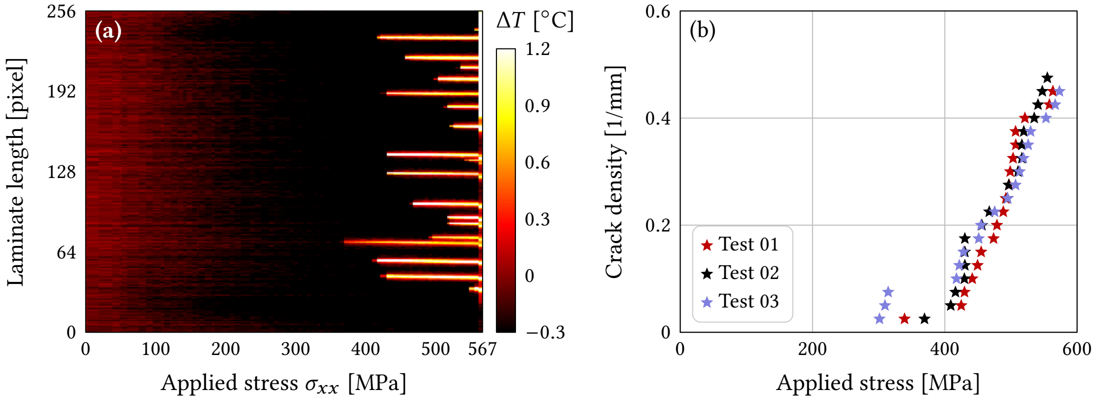

Figure 8 Crack density for a $[0/90_2]_s$ laminate subject to tensile tests performed at 0.1 m/s: (a) captured thermal events for Test 02 and (b) crack kinetics

Figure 9 Captured thermal events for a $[0/90_2]_s$ laminate subject to tensile tests performed at 1.4 m/s.

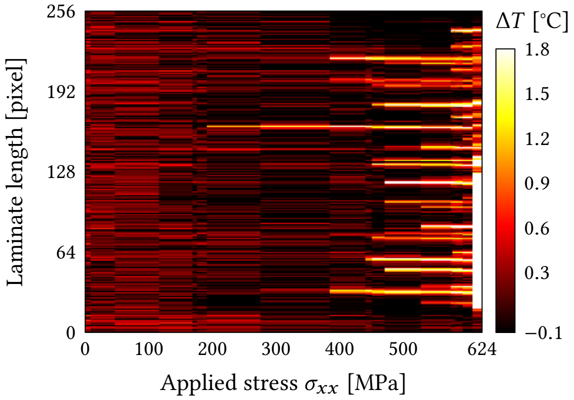

8(b) clearly exhibit a relatively low scattering of the experimental results. It can also be noticed that the spatial cracks distribution seems to be unaffected by the loading rate increase. The cracks are still spread through the free length in a random way. Table 2 quantifies the considered mechanism.

Loading rates	σ_{onset} [MPa]	$\varepsilon_{\text{onset}}$ (%)	$d^{\max}$ (mm^{-1})	$\sigma_{xx}^{d_{\max}}$ [MPa]	$\varepsilon_{xx}^{d_{\max}}$ (%)
5 mm/min	383.9 ± 7.83 %	0.84 ± 7.71 %	0.54 ± 0.04	574.42 ± 4.30 %	1.32 ± 3.30 %
50 mm/min	332.7 ± 10.63 %	0.73 ± 10.48 %	0.55 ± 0.03	582.47 ± 3.62 %	1.34 ± 4.10 %
500 mm/min	385.5 ± 13.5 %	0.84 ± 15.30 %	0.50 ± 0.04	590.58 ± 4.65 %	1.34 ± 4.31 %
0.1 m/s	336.6 ± 10.1 %	0.74 ± 10.08 %	0.46 ± 0.02	563.92 ± 1.63 %	1.30 ± 2.35 %

Table 2 Crack kinetics results using the IR thermal protocol for the $[0/90_2]_s$ laminate at several loading rates.

The results exhibit a very low scatter regarding the maximum crack density as well as the

$\sigma_{xx}^{d_{\max}}$ stress and the $\varepsilon_{xx}^{d_{\max}}$ strain levels corresponding to the last detected crack. As expected, a larger scattering is observed for the stress threshold at the onset of the first crack. Similarly to the thicker laminates tested up to 500 mm/min in (Berthe and Ragonet 2018), no rate effects seem to emerge for this stacking sequence over the same range of loading rate and up to 0.1 m/s.

The methodology described in this section presents therefore the benefits of being simple from a post-processing point of view and for the interpretation of the data. The reliability of the procedure has been demonstrated over a wide range of loading rates. Moreover, this methodology gives access to a continuous measurement correlated to the spatial distribution of the cracks as a function of the stress applied to the specimen at several loading rates which can be useful for the validation of the constitutive laws. In the sequel, the same procedure is applied to the other three laminate configurations in order to assess the capability of the presented methodology to be applied to different cross-ply laminate thicknesses.

3.2 Influence of the ply thickness on the rate dependency of crack density evolution

Based on the experimental protocol and the previously presented methodology, the influence of 90° ply thickness on the rate effect of the transverse crack kinetics is assessed. First of all, the results obtained with the thinner $[0/90_{1/2}]_s$ laminate configuration have been proven to be the current limit of this protocol due to the experimental setup and camera configuration chosen for this experimental investigation. Indeed an insufficient amount of pixels (*i.e.* one pixel) located in the thickness of the 90° ply is obtained with the selected free-length and camera lens. This low spatial resolution does not ensure a consistent detection of the crack occurrences, hence the thinner configuration considered in the present study is withdrawn of the following analysis. By using samples of smaller free-length and another camera lens, the spatial resolution can be increased and this limitation might be overcome. Despite this limitation, Figures 10 and 11 illustrate the results from the proposed procedure applied to the configurations $[0/90_3]_s$ at 0.1 m/s and $[0/90_1]_s$ for each loading-rate, where the number of pixels in the thickness of the 90° plies is fixed at 9 pixels and 3 pixels respectively, regardless of the considered loading rate for this study.

Figure 10 Captured thermal events for a $[0/90_3]_s$ laminate subject to a tensile test performed at 0.1 m/s.

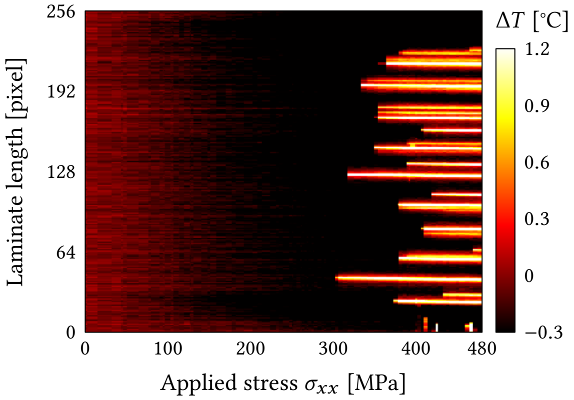

These figures clearly exhibit that the crack mechanism remains well captured for both laminate configurations over the whole range of loading rates. With the method proposed in this paper, a direct comparison between the thicker and the thinner laminate configurations can be established. As it can be qualitatively observed, the lower the number of 90° plies, the higher the crack density and the stress threshold regarding the onset of the first crack. These trend is quantitatively depicted in Figure 12 where every tensile tests performed at a loading rate of 5 mm/min are reported for each tested laminate configuration. For the $[0/90_3]_s$ configuration, the results used in the present study for the loading rates between 5 mm/min and 500 mm/min are extracted from (Berthe and Ragonet 2018).

For the thickest configuration, the average of the maximum crack density is estimated at $d^{\max} = 0.59 \pm 0.05$ upon reaching an average mean stress value estimated at $\sigma_{xx}^{d_{\max}} = 488.96\,\text{MPa} \pm 8.37\,\%$ and a stress threshold for crack onset at a mean value of about $\sigma_{\text{onset}} = 294.37\,\text{MPa} \pm 6.73\,\%$. For the thinnest configuration, the average of the maximum crack density is estimated at $d^{\max} = 0.95 \pm 0.11$

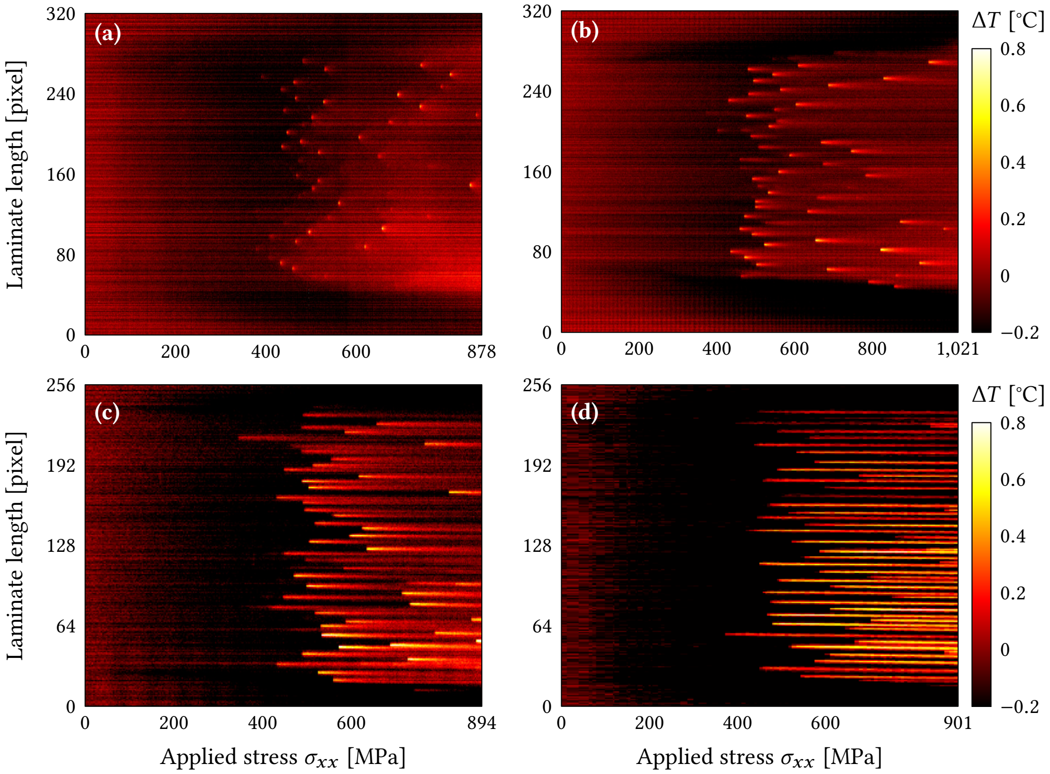

Figure 11 Captured thermal events for a $[0/90_1]_s$ laminate subject to tensile tests performed at several loading rates: (a) 5 mm/min, (b) 50 mm/min, (c) 500 mm/min and (d) 0.1 m/s. Same colorbar for all figures.

Figure 12 Thickness effect on the crack density captured with the IR protocol and based on tensile tests performed at 5 mm/min.

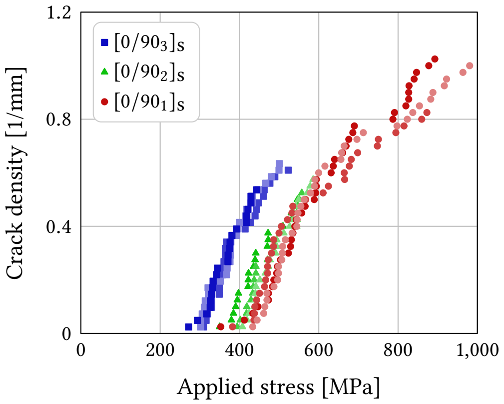

upon reaching an average mean stress value estimated at $\sigma_{xx}^{d_{\max}}$ = 915.33 MPa ± 6.27 % and a stress threshold for crack onset at a mean value of about σ_{onset} = 389.62 MPa ± 10.45 %. On the other hand, the intermediate $[0/90_2]_s$ laminate configuration is consistently located between the two others although it can be seen that the maximum crack density appears to be slightly lower than the thicker configuration. Finally, these trends are in agreement with those reported in (Parvizi et al. 1978; Nairn 2000; Berthelot 2003), which increases the confidence in the proposed IR thermal detection protocol.

The loading rate sensitivity is analysed in the sequel. The stress–strain responses for the different loading rates are plotted in Figure 13. For the three different laminate configurations, the subfigures include the three tests performed for each loading rate in order to assess the low experimental scattering. On the one hand, no rate effect is clearly emphasized regarding the macroscopic behavior over the considered range of loading rates. On the other hand, and as expected, the lower the number of 90° plies, the greater macroscopic failure stress. Respectively to each laminate configuration, the failure stress can be considered as rate-insensitive. These two aspects suggest that most of the mechanical contribution to the macroscopic behavior for these cross-ply configurations can be attributed to the outer 0° plies, whose rate-insensitivity is well known. This assumption seems to be also confirmed by the values obtained in the present study

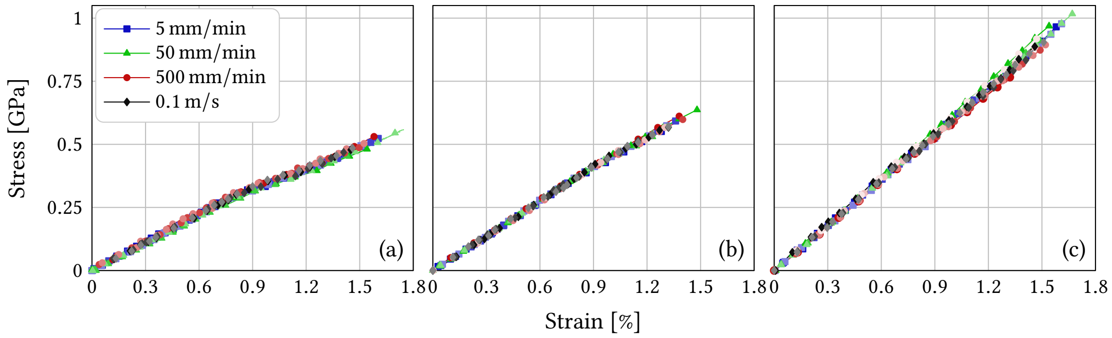

Figure 13 Macroscopic tensile behavior of the laminate configurations: (a) $[0/90_3]_s$, (b) $[0/90_2]_s$ and (c) $[0/90_1]_s$.

for the maximum strain applied to the laminate and summarized in Table 3.

	$[0/90_1]_s$		$[0/90_2]_s$		$[0/90_3]_s$	
Loading rates	$\sigma_{\max}$ [MPa]	$\varepsilon_{\max}$	$\sigma_{\max}$ [MPa]	$\varepsilon_{\max}$	$\sigma_{\max}$ [MPa]	$\varepsilon_{\max}$
5 mm/min	959.54 ± 7.38 %	1.65×10^{-2} ± 6.98 %	602.45 ± 1.97 %	1.38×10^{-2} ± 1.5 %	514.94 ± 3.96 %	1.57×10^{-2} ± 4.51 %
50 mm/min	970.63 ± 4.43 %	1.58×10^{-2} ± 4.74 %	600.91 ± 5.81 %	1.40×10^{-2} ± 6.9 %	513.51 ± 7.80 %	1.66×10^{-2} ± 6.66 %
500 mm/min	869.34 ± 7.56 %	1.49×10^{-2} ± 7.00 %	594.61 ± 4.74 %	1.37×10^{-2} ± 4.9 %	510.09 ± 3.11 %	1.54×10^{-2} ± 4.76 %
0.1 m/s	889.91 ± 4.05 %	1.48×10^{-2} ± 3.04 %	571.46 ± 1.19 %	1.33×10^{-2} ± 1.30 %	497.96 ± 2.41 %	1.46×10^{-2} ± 3.13 %

Table 3 Ultimate macroscopic tensile properties of the tested laminate configurations.

Finally, the crack density is plotted in Figure 14 in terms of the applied stress, for the considered loading rates and for each laminate configuration. This figure includes the three tests performed for each loading rate in order to assess the low experimental scattering. As observed in Figures 14(a) and 14(b), the crack density and its kinetic appear to be rate-insensitive over the wide range of loading rates considered in this paper. On the contrary, Figure 14(c) clearly exhibits a rate dependency of the transverse cracking evolution. For the $[0/90_1]_s$ laminate, the crack density evolution appears to be accelerated particularly between $\sigma_{xx} = 400$ MPa and $\sigma_{xx} = 500$ MPa with the loading rate increase. Consequently, the maximum crack density reaches a higher value for the two higher loading rates (*i.e.* 500 mm/min and 0.1 m/s) than for the two lower loading rates (*i.e.* 5 mm/min and 50 mm/min). We can finally notice that the higher the loading rate, the lower the $\sigma_{xx}^{d_{\max}}$. It can be concluded that the thickness of cross-ply laminate have a significant influence on the rate effect of the transverse cracking mechanism. In spite of this conclusion and contrary to (Nguyen et al. 2015), the stress at which the first crack appeared seems to be rate-insensitive in the present study. It is the same tendency for the deformation at which the first crack appears. The quantitative synthesis of these trends is provided in Table 4.

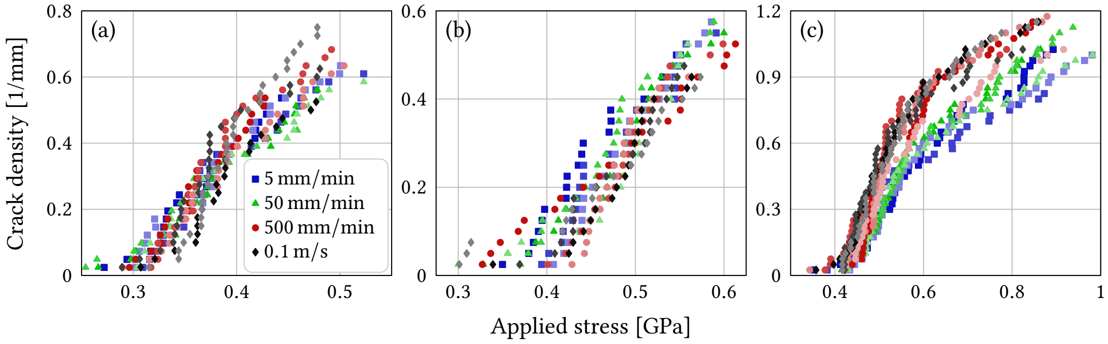

Figure 14 Quantified crack density for the laminate configurations: : (a) $[0/90_3]_s$, (b) $[0/90_2]_s$ and (c) $[0/90_1]_s$.

3.3 Discussions

On the one hand, the origin of the emphasized loading-rate effect on the thinner stacking sequence might be explained from an energetic point of view. As firstly observed by Parvizi et al. (1978)

$[0/90_3]_s$						
Loading rates	$\dot{\varepsilon}$ $[\mathrm{s}^{-1}]$	σ_{onset} [MPa]	$\varepsilon_{\mathrm{onset}}$	$d^{\max}$ $[\mathrm{mm}^{-1}]$	$\sigma_{xx}^{d_{\max}}$ [MPa]	$\varepsilon_{xx}^{d_{\max}}$
5 mm/min	8.3×10^{-4}	294.4 ± 6.74 %	0.0080 ± 9.21 %	0.59 ± 0.05	488.96 ± 8.37 %	0.015 ± 8.25 %
50 mm/min	6.4×10^{-3}	274.7 ± 9.50 %	0.0079 ± 8.83 %	0.53 ± 0.08	486.59 ± 6.79 %	0.016 ± 6.62 %
500 mm/min	4.6×10^{-2}	301.0 ± 4.76 %	0.0081 ± 7.11 %	0.62 ± 0.07	474.40 ± 8.66 %	0.014 ± 9.94 %
0.1 m/s	0.78	303.9 ± 4.38 %	0.0082 ± 3.82 %	0.63 ± 0.11	478.56 ± 0.38 %	0.014 ± 0.80 %
$[0/90_2]_s$						
5 mm/min	8.1×10^{-4}	383.9 ± 7.83 %	0.0084 ± 7.71 %	0.54 ± 0.04	574.42 ± 4.30 %	0.013 ± 3.30 %
50 mm/min	6.5×10^{-3}	332.7 ± 10.63 %	0.0073 ± 10.5 %	0.55 ± 0.03	582.47 ± 3.62 %	0.013 ± 4.10 %
500 mm/min	4.0×10^{-2}	385.5 ± 13.5 %	0.0084 ± 15.3 %	0.50 ± 0.04	590.58 ± 4.65 %	0.014 ± 4.32 %
0.1 m/s	0.79	336.6 ± 10.1 %	0.0074 ± 10.1 %	0.46 ± 0.02	563.92 ± 1.63 %	0.013 ± 2.35 %
$[0/90_1]_s$						
5 mm/min	9.1×10^{-4}	389.6 ± 10.45 %	0.0065 ± 11.1 %	0.95 ± 0.11	915.33 ± 6.27 %	0.015 ± 6.02 %
50 mm/min	7.5×10^{-3}	424.2 ± 1.83 %	0.0070 ± 2.38 %	1.04 ± 0.04	912.37 ± 6.78 %	0.015 ± 6.57 %
500 mm/min	4.1×10^{-2}	381.5 ± 10.5 %	0.0065 ± 10.6 %	1.12 ± 0.08	878.84 ± 5.53 %	0.015 ± 7.19 %
0.1 m/s	0.79	398.9 ± 9.0 %	0.0066 ± 11.5 %	1.11 ± 0.07	846.42 ± 2.30 %	0.014 ± 1.08 %

Table 4 Crack kinetics results using the IR thermal protocol.

regarding cross-ply glass fiber reinforced polymers and well summarized by Leguillon (2002), as long as the 90° ply thickness remains sufficiently thick, the onset of the transverse cracking occurrence appears for a constant strain and could be predicted with a stress criterion based on a constant stress value. Below a critical thickness, the applied stress must be increased and a stress criterion for the onset of crack occurrence can no longer be considered consistent compared to an energy criterion based on the mode I fracture toughness G_c. A considerable amount of work has been performed regarding the rate dependency of the G_c fracture toughness (Yaniv and Daniel 1988; Hug et al. 2006; Isakov et al. 2019; Azadi et al. 2019), although there is no consensus regarding its rate dependency. This is mainly due to the fact that the G_c characterization tests are not normalized for high speed loading (May 2016) leading to inconsistent trends for which results are highly dependent on the protocol. In order to nonetheless develop the line of reasoning, we note that a few studies conclude that increasing loading rates would lead to a decrease in G_c (Kusaka et al. 1998; Zabala et al. 2015; Thorsson et al. 2018). Considering this aspect, Laws and Dvorak (1988) showed, by means of an analytical prediction, that the tougher the material the less the crack density for a given applied load. Consequently, the decrease of G_c with the loading rate increase may explain the maximum crack density increased $d^{\max}$ and the associated $\sigma_{xx}^{d_{\max}}$ decreased.

On the other hand, a loading rate effect can also be observed on the thicker configuration. With the loading rate increase, the shape of the cracks evolves and curved/oblique cracks can be observed for the higher loading speed, as shown in Figure 15. Curved cracks classically appear when the 90° ply thickness increase (Groves et al. 1987; Allen et al. 1988). Only a few studies deal with this specific mechanism. This phenomenon would appear as consequence to the saturation of the transverse cracking mechanism (Hu et al. 1993) or due to the difference in toughness between mode I and mode II for a given material (Jalalvand et al. 2014). In this study, curved cracks appear for the configuration with six 90° plies but only for higher loading rates. This phenomenon might also be a consequence of a material rate dependency which is observed for this configuration on the matrix cracking pattern and no longer observed on matrix crack density evolution.

4 Conclusions

This study aimed at assessing the experimental capability of an infrared thermal protocol to capture and accurately quantify the evolution of transverse matrix cracking in cross-ply laminates subject to various loading rates, from quasi-static to intermediate loading rates. Various laminate thicknesses were considered in order to assess the influence of the 90° plies on the rate dependency of the crack mechanism. The proposed protocol for detecting the matrix cracking mechanism by

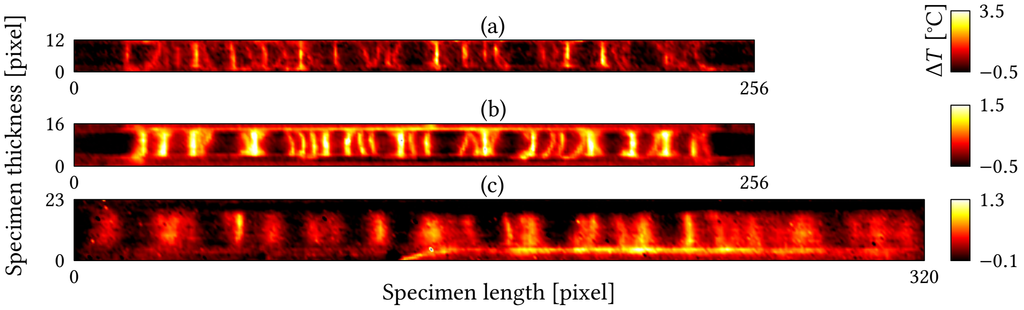

Figure 15 Transverse cracking pattern on a the $[0/90_3]_s$ laminate prior the final failure of the specimen subject to various loading rates: (a) 1.4 m/s, (b) 0.1 m/s and (c) 500 mm/min.

infrared thermography was validated over a wide range of loading rates. By means of a simple analysis methodology of the thermal data, proven to be valid irrespective of the loading rate, it is possible to get access to an objective and accurate representation of the evolution of the crack density over the whole free length of the specimen and directly as a function of the applied stress until the final failure. The trends associated to thickness effects are in agreement with the literature. Focusing on the investigated material and the considered range of loading rates, this study emphasizes that a rate dependency of the crack density evolution with respect to the applied stress can be observed only for the $[0/90_1]_s$ laminate. For this configuration, the increase of the loading rate leads to an increase of the maximum crack density without affecting the onset threshold of the mechanism. The observed rate dependency has to be further investigated in order to better understand the threshold effect driven by the 90° ply thickness and leading to an observable rate dependency of the matrix crack density evolution.

References

Allen, D., C. Harris, S. Groves, and R. Norvell (1988). Characterization of stiffness loss in crossply laminates with curved matrix cracks. *Journal of Composite Materials* 22(1):71–80. [DOI].

Azadi, M., M. Saeedi, M. Mokhtarishirazabad, and P. Lopez-Crespo (2019). Effects of loading rate on crack growth behavior in carbon fiber reinforced polymer composites using digital image correlation technique. *Composites Part B: Engineering* 175:107161. [DOI].

Battams, G. and J. Dulieu-Barton (2016). Data-rich characterisation of damage propagation in composite materials. *Composites Part A: Applied Science and Manufacturing* 91:420–435. [DOI], [OA].

Berthe, J. and M. Ragonet (2018). Passive infrared thermography measurement of transverse cracking evolution in cross-ply laminates. *Strain* 54(6):e12293. [DOI], [HAL].

Berthelot, J.-M. (2003). Transverse cracking and delamination in cross-ply glass-fiber and carbon-fiber reinforced plastic laminates: static and fatigue loading. *Applied Mechanics Reviews* 56(1):111–147. [DOI].

Crossman, F., W. Warren, A. Wang, and G. Law (1980). initiation and growth of transverse cracks and edge delamination in composite laminates Part 2. Experimental correlation. *Journal of Composite Materials* 14(1):88–108. [DOI].

Dzenis, Y. (2003). Cycle-based analysis of damage and failure in advanced composites under fatigue: 1. Experimental observation of damage development within loading cycles. *International Journal of Fatigue* 25(6):499–510. [DOI].

Farge, L., J. Varna, and Z. Ayadi (2010). Damage characterization of a cross-ply carbon fiber/epoxy laminate by an optical measurement of the displacement field. *Composites Science and Technology* 70(1):94–101. [DOI].

Groves, S. E., C. E. Harris, A. L. Highsmith, D. H. Allen, and R. G. Norvell (1987). An experimental and analytical treatment of matrix cracking in cross-ply laminates. *Experimental Mechanics* 27(1):73–79. [DOI].

Hu, S., J. Bark, and J. Nairn (1993). On the phenomenon of curved microcracks in $[(S)/90_n]_s$ laminates: Their shapes, initiation angles and locations. *Composites Science and Technology*

47(4):321–329. [doi].

Huchette, C. (2005). Sur la complémentarité des approches expérimentales et numériques pour la modélisation des mécanismes d'endommagement des composites stratifiés. PhD thesis. Paris VI. [hal].

Hug, G., P. Thévenet, J. Fitoussi, and D. Baptiste (2006). Effect of the loading rate on mode I interlaminar fracture toughness of laminated composites. *Engineering Fracture Mechanics* 73(16):2456–2462. [doi].

Isakov, M., M. May, P. Hahn, H. Paul, and M. Nishi (2019). Fracture toughness measurement without force data. Application to high rate DCB on CFRP. *Composites Part A: Applied Science and Manufacturing* 119:176–187. [doi].

Jalalvand, M., M. Wisnom, H. Hosseini-Toudeshky, and B. Mohammadi (2014). Experimental and numerical study of oblique transverse cracking in cross-ply laminates under tension. *Composites Part A: Applied Science and Manufacturing* 67:140–148. [doi], [oa].

Kusaka, T., M. Hojo, Y.-W. Mai, T. Kurokawa, T. Nojima, and S. Ochiai (1998). Rate dependence of mode I fracture behaviour in carbon-fibre/epoxy composite laminates. *Composites Science and Technology* 58(3-4):591–602. [doi].

Laws, N. and G. Dvorak (1988). Progressive transverse cracking in composite laminates. *Journal of Composite Materials* 22(10):900–916. [doi].

Leguillon, D. (2002). Strength or toughness? A criterion for crack onset at a notch. *European Journal of Mechanics - A/Solids* 21(1):61–72. [doi], [hal].

Li, Y., Z.-W. Yang, J.-T. Zhu, A.-B. Ming, W. Zhang, and J.-Y. Zhang (2016). Investigation on the damage evolution in the impacted composite material based on active infrared thermography. *NDT & E International* 83:114–122. [doi].

Lisle, T., C. Bouvet, M. Pastor, P. Margueres, and R. Prieto Corral (2013). Damage analysis and fracture toughness evaluation in a thin woven composite laminate under static tension using infrared thermography. *Composites Part A: Applied Science and Manufacturing* 53:75–87. [doi], [hal].

May, M. (2016). Measuring the rate-dependant mode I fracture toughness of composite - A review. *Composites Part A: Applied Science and Manufacturing* 81:1–12. [doi].

Meola, C. and G. Carlomagno (2009). Infrared thermography of impact-driven thermal effects. *Applied Physics A* 96(3):759–762. [doi].

Montesano, J., H. Bougherara, and Z. Fawaz (2014). Application of infrared thermography for the characterization of damage in braided carbon fiber reinforced polymer matrix composites. *Composites Part B: Engineering* 60:137–143. [doi].

Nairn, J. (2000). Matrix Microcracking in Composites. *Comprehensive Composite Materials.* Ed. by A. Kelly and C. Zweben. Pergamon, pp 403–432. [doi].

Nguyen, T. H., D. Gamby, and M.-C. Lafarie-Frenot (2015). Loading rate effect on matrix transverse cracking in aeronautical CFRP composite laminates. [hal].

Parvizi, A., K. W. Garrett, and J. E. Bailey (1978). Constrained cracking in glass fibre reinforced epoxy cross-ply laminates. *Journal of Materials Science* 13(1):195–201. [doi].

Portemont, G., J. Berthe, A. Deudon, and F.-X. Irisarri (2018). Static and dynamic bearing failure of carbon/epoxy composite joints. *Composite Structures* 204:131–141. [doi], [hal].

Thorsson, S., A. Waas, J. Schaefer, B. Justusson, and S. Liguore (2018). Effects of elevated loading rates on mode I fracture of composite laminates using a modified wedge-insert fracture method. *Composites Science and Technology* 156:39–47. [doi].

Toubal, L., M. Karama, and B. Lorrain (2006). Damage evolution and infrared thermography in woven composite laminates under fatigue loading. *International Journal of Fatigue* 28(12):1867–1872. [doi].

Yaniv, G. and I. M. Daniel (1988). Height-tapered double cantilever beam specimen for study of rate effects on fracture toughness of composites. *8th Conference on Composite Materials Testing and Design.* ASTM International, pp 241–258. [doi].

Zabala, H., L. Aretxabaleta, G. Castillo, and J. Aurrekoetxea (2015). Loading rate dependancy on mode I interlaminar fracture toughness of unidrectional and woven carbon fibre epoxy composites. *Composite Structures* 121:75–82. [doi].

Authors' contributions F.C.: Investigation, Post-treatment, Writing, Review and Editing. J.B.: Conceptualization, Post-treatment, Writing, Review and Editing. M.R.: Investigation, Post-treatment. All the authors discussed the results and proposed corrections.

Supplementary Material None.

Acknowledgements The authors gratefully acknowledge the funding from the French Civil Aviation Directorate (DGAC). They also gratefully acknowledge the Hauts-de-France Region for funding equipment that contributed to this research work.

Ethics approval and consent to participate Not applicable.

Consent for publication Not applicable.

Competing interests The authors declare that they have no competing interests.